

A Scaler-Based Data Acquisition System for Measuring Parity-Violating Asymmetry in Deep Inelastic Scattering

R. Subedi^{a,1}, D. Wang^a, K. Pan^b, X. Deng^a, R. Michaels^c,
P. E. Reimer^d, A. Shahinyan^e, B. Wojtsekhowski^c, X. Zheng^{a,*}

^a*University of Virginia, Charlottesville, VA 22904, USA*

^b*Massachusetts Institute of Technology, Cambridge, MA 02139, USA*

^c*Thomas Jefferson National Accelerator Facility, Newport News, VA 23606, USA*

^d*Physics Division, Argonne National Laboratory, Argonne, IL 60439, USA*

^e*Yerevan Physics Institute, Yerevan 0036, Armenia*

Abstract

An experiment that measured the parity-violating asymmetries in deep inelastic scattering was completed at the Thomas Jefferson National Accelerator Facility in experimental Hall A. From these asymmetries, a combination of the quark weak axial charge could be extracted with a factor of five improvement in precision over world data. To achieve this, asymmetries at the 10^{-4} level needed to be measured at event rates up to 600 kHz and the high pion background typical to deep inelastic scattering experiments needed to be rejected efficiently. A specialized data acquisition (DAQ) system with intrinsic particle identification (PID) was successfully developed and used: The pion contamination in the electron samples was controlled at the order of 2×10^{-4} or below with an electron efficiency of higher than 91% during most of the production period of the experiment, the systematic uncertainty in the measured asymmetry due to DAQ deadtime was below 0.5%, and the statistical quality of the asymmetry measurement agreed with the Gaussian distribution to over five orders of magnitudes. The DAQ system is presented here with an emphasis on its design scheme, the achieved PID performance, deadtime effect and the capability of measuring small asymmetries.

Key words: Jefferson Lab; Hall A; PVDIS; DAQ

PACS: 11.30.Er, 12.15.Mm, 13.60.Hb 14.60.Cd 14.65.Bt 29.30.Aj 29.85.Ca

¹ Present address: Richland College, Dallas County Community College District, Dallas, Texas 75243, USA

* Corresponding author. E-mail: xiaochao@jlab.org; Telephone: 001-434-243-4032; Fax: 001-434-924-4576

29 **1 Introduction**

30 The Parity-Violating Deep Inelastic Scattering (PVDIS) experiment E08-011 was
 31 completed in December 2009 at the Thomas Jefferson National Accelerator Facil-
 32 ity (JLab). The goal of this experiment [1,2,3] was to measure with high precision
 33 the parity-violating asymmetry in deep inelastic scattering of a polarized 6 GeV
 34 electron beam on an unpolarized liquid deuterium target. This asymmetry is sensi-
 35 tive to the quark weak axial charge C_{2q} which corresponds to a helicity dependence
 36 in the quark coupling with the Z^0 boson.

37 For electron inclusive scattering from an unpolarized target, the electromagnetic
 38 interaction is parity conserving and is insensitive to the spin flip of the incom-
 39 ing electron beam. Only the weak interaction violates parity and causes a differ-
 40 ence between the right- and the left-handed electron scattering cross-sections σ_R
 41 and σ_L . The dominant contribution to the parity violation asymmetry, $A_{PV} \equiv$
 42 $(\sigma_R - \sigma_L)/(\sigma_R + \sigma_L)$, arises from the interference between electromagnetic and
 43 weak interactions and is proportional to the four momentum transfer squared Q^2
 44 for $Q^2 \ll M_Z^2$. The magnitude of the asymmetry is on the order of 10^{-4} or 10^2 parts
 45 per million (ppm) at $Q^2 = 1$ (GeV/c) 2 .

46 The PVDIS asymmetry from a deuterium target is [4]

$$A_{PV} = \left(-\frac{G_F Q^2}{4\sqrt{2}\pi\alpha} \right) \left(2g_A^e Y_1 \frac{F_1^{\gamma Z}(x, Q^2)}{F_1^\gamma(x, Q^2)} + g_V^e Y_3 \frac{F_3^{\gamma Z}(x, Q^2)}{F_1^\gamma(x, Q^2)} \right), \quad (1)$$

47 where Q^2 is the negative of the four-momentum transfer squared, G_F is the Fermi
 48 weak coupling constant, α is the fine structure constant, Y_1 and Y_3 are kinematic
 49 factors, x is the Bjorken scaling variable, and $F_{1,3}^{\gamma(Z)}(x, Q^2)$ are deuteron structure
 50 functions that can be evaluated from the parton distribution functions and the quark-
 51 Z^0 vector and axial couplings $g_{V,A}^q$. From this asymmetry one can extract the quark
 52 weak vector and axial charges $C_{1,2q}$, where the quark weak vector charge is defined
 53 as $C_{1q} \equiv 2g_A^e g_V^q$ and the quark weak axial charge is given by $C_{2q} \equiv 2g_V^e g_A^q$ with
 54 $q = u, d$ indicating an up or a down quark, $g_{A(V)}^e$ is the electron axial (vector)
 55 coupling and $g_{V(A)}^q$ is the quark vector (axial) coupling to the Z^0 boson. In the tree-
 56 level Standard Model, the $C_{1,2q}$ are related to the weak mixing angle θ_W : $C_{1u} =$
 57 $-\frac{1}{2} + \frac{4}{3} \sin^2 \theta_W$, $C_{2u} = -\frac{1}{2} + 2 \sin^2 \theta_W$, $C_{1d} = \frac{1}{2} - \frac{2}{3} \sin^2 \theta_W$, and $C_{2d} = \frac{1}{2} -$
 58 $2 \sin^2 \theta_W$. Although the weak mixing angle and the quark weak vector charge C_{1q}
 59 have been measured from various processes [5], the current knowledge of the quark
 60 weak axial charge C_{2q} is poor and their deviations from the Standard Model value
 61 would reveal possible New Physics in the quark axial couplings that could not be
 62 accessed from other Standard Model parameters.

63 The goal of JLab E08-011 was to measure the PVDIS asymmetries to statistical
 64 precisions of 3% and 4% at $Q^2 = 1.1$ and 1.9 (GeV/c) 2 , respectively, and under the

65 assumption that hadronic physics corrections are small, to extract the quark axial
 66 weak charge combination ($2C_{2u} - C_{2d}$). In addition, the systematic uncertainty
 67 goal was less than 3%. For this experiment, the expected asymmetries were 91 and
 68 160 ppm respectively at the two Q^2 values [1]. To achieve the required precision,
 69 an event rate capability of up to 600 kHz was needed.

70 The main challenge of deep inelastic scattering experiments is the separation of
 71 scattered electrons from the pion background in the spectrometer and detector sys-
 72 tem. The neutral pions would decay into e^+e^- pairs from which the electrons pro-
 73 duced cannot be rejected by detectors. This pair production background was studied
 74 by reversing the spectrometer magnet settings and measure the e^+ yield, and the ef-
 75 fect on the measured asymmetries was found to be negligible. Charged pions are
 76 produced primarily from nucleon resonance decays and could carry a parity vio-
 77 lation asymmetry corresponding to the Q^2 at which the resonances are produced,
 78 typically a fraction of the asymmetry of electrons with the same scattered momen-
 79 tum. Assuming that a fraction $f_{\pi/e}$ of the detected events are π^- and $1 - f_{\pi/e}$ are
 80 electrons, the measured asymmetry is

$$A_m = f_{\pi/e}A_\pi + (1 - f_{\pi/e})A_e, \quad (2)$$

81 where A_e is the desired electron scattering asymmetry and A_π is the asymmetry of
 82 the pion background. To extract A_e to a high precision, one needs either to mini-
 83 mize the pion contamination $f_{\pi/e}$ to a negligible level, or to correct the measured
 84 asymmetry for the asymmetry of pions, which itself needs to be measured precisely.
 85 For the PVDIS experiment, the goal was to control $f_{\pi/e}$ to the 10^{-4} level provided
 86 that the pion asymmetries did not exceed those of electrons.

87 The experiment used a 100 μ A electron beam with a polarization of approximately
 88 90% and a 20-cm long liquid deuterium target. The two High Resolution Spec-
 89 trometers (HRS) [6] were used to detect scattered events. While the standard HRS
 90 detector package and data acquisition (DAQ) system routinely provide a 10^4 pion
 91 rejection with approximately 99% electron efficiency, they are based on full record-
 92 ing of the detector signals and are limited to event rates up to 4 kHz [6]. This is not
 93 sufficient for the high rates expected for the experiment. (The HRS DAQ will be
 94 referred to as “standard DAQ” hereafter.)

95 Recent parity violation electron scattering experiments, such as HAPPEX [8,9,10,11,12],
 96 and PREX [13] at JLab, focused on elastic scattering from nuclear or nucleon tar-
 97 gets that are typically not contaminated by inelastic backgrounds. Signals from the
 98 detectors can be integrated and a helicity dependence in the integrated signal can
 99 be used to extract the physics asymmetry. An integrating DAQ was also used in
 100 the preceding PVDIS measurement at SLAC [14,15] in which approximately 2%
 101 of the integrated signal was attributed to pions. The SAMPLE experiment [7] at
 102 MIT-Bates focused also on elastic scattering but the inelastic contamination was
 103 more challenging to reject, and an air Cherenkov counter was used to select only

104 elastic scattering events. In the Mainz PVA4 experiment [16,17,18], particles were
105 detected in a total absorption calorimeter and the integrated energy spectrum was
106 recorded. Charged pions and other background were separated from electrons in
107 the offline analysis of the energy spectrum, and the pion rejection was on the order
108 of 100:1 based on the characteristics of the calorimeter.

109 High performance particle identification can usually be realized in a counting-based
110 DAQ where each event is evaluated individually. In the G0 experiment [19,20,21,22,23]
111 at JLab, a superconducting spectrometer with a 2π azimuthal angle coverage was
112 used to detect elastically scattered protons at the forward angle and elastic elec-
113 trons at the backward angle. At the forward angle, protons were identified using
114 time-of-flight. At the backward angle, pions were rejected from electrons using an
115 aerogel Cherenkov counter, and a pion rejection factor of 125 : 1 or better was
116 reported [23]. The deadtime correction of the counting system was on the order of
117 a few percent [22,23].

118 While the PVDIS experiment could fully utilize existing spectrometers and detec-
119 tors at JLab, examination of all existing techniques for PV measurements made it
120 clear that a custom electronics and DAQ were needed to keep the systematic uncer-
121 tainties due to data collection to below 1%. In this paper we describe a scaler-based,
122 cost effective counting DAQ which limited the pion contamination of the data sam-
123 ple to a negligible level of $f_{\pi/e} \approx 10^{-4}$. Basic information on the detector package
124 and the DAQ setup will be presented first and followed by the analysis of electron
125 detection efficiency, pion rejection and contamination, corrections due to counting
126 deadtime, and the statistical quality of the asymmetry measurement.

127 **2 Detector and DAQ Overview**

128 The design goal of the DAQ is to record data up to 600 kHz with hardware-based
129 PID and well measured and understood deadtime effects. The following detectors
130 in the HRS [6] were used to characterize scattered particles: Two scintillator planes
131 provided the main trigger, while a CO₂ gas Cherenkov detector and a double-layer
132 segmented lead-glass detector provided particle identification information. The ver-
133 tical drift chambers (as the tracking detector) were used during calibration runs but
134 were turned off during production data taking because they were not expected to
135 endure the high event rates.

136 For the gas Cherenkov and the lead-glass detector, a full recording of their out-
137 put ADC data was not feasible at the expected high rate. Instead their signals were
138 passed through discriminators and logic units to form preliminary electron and pion
139 triggers. These preliminary triggers were then combined with the scintillator trig-
140 gers to form the final electron and pion triggers, which were sent to scalars to record
141 the event counts and used offline to form asymmetries $A = (n_R - n_L)/(n_R + n_L)$,

142 where $n_{R(L)}$ is the integrated rate of the triggers normalized to the integrated beam
143 charge for the right(R) and left(L) handed spin (helicity) states of the incident
144 electron beam. The scalers that counted triggers and the beam charge were inte-
145 grated over the helicity period, which was flipped pseudo-randomly at 30 Hz per
146 the experimental technique used by the HAPPEX experiments [12].

147 For the HRS the two layers of the lead-glass detector are called “preshower” and
148 “shower” detectors, respectively. The preshower in the Right HRS (the spectrome-
149 ter located to the right side of the beamline when viewed along the beam direction)
150 has 48 blocks arranged in a 2×24 array, with the longest dimension of the blocks
151 aligned perpendicular to the particle trajectory. For the two blocks in each row, only
152 the ends facing outward are read out by photo-multiplier tubes (PMTs), while the
153 other ends of the two blocks are facing each other and not read out. Therefore, the
154 preshower detector has 48 output channels. All preshower blocks were individually
155 wrapped to prevent light leak. The shower detector in the Right HRS had 75 blocks
156 arranged in a 5×15 array with the longest dimension of the blocks aligned along
157 the trajectory of scattered particles. PMTs were attached to each block of the Right
158 shower detector on one end only, giving normally 75 output channels. However to
159 minimize the electronics needed for this experiment (see next paragraph), only 60
160 of the 75 shower blocks were used while signals from the 15 blocks on the edge
161 were not utilized by the DAQ. The reduction of the HRS acceptance due to not
162 using these side blocks was negligible. The preshower and the shower detectors in
163 the Left HRS are similar to the preshower detector on the Right HRS except that
164 for each detector there are 34 blocks arranged in a 2×17 array.

165 Because the lead-glass detectors in the Left and Right HRS are different, design of
166 the lead-glass-based triggers of the DAQ is also different, as shown in Fig. 1. As a
167 compromise between the amount of electronics needed and the rate in the front end
168 logic modules, the lead-glass blocks in both the preshower and the shower detectors
169 were divided into 6 (8) groups for the Left (Right) HRS, with each group consist-
170 ing typically 8 blocks. Signals from the 8 blocks in each group were added using a
171 custom-made analog summing unit called the “SUM8 module”, then passed to dis-
172 criminators. The geometry and the position of each preshower group were carefully
173 chosen to match those of the corresponding shower group to maximize electron de-
174 tection efficiency. On the Left HRS, adjacent groups in both preshower and shower
175 had overlapping blocks, while for the Right HRS only preshower groups were over-
176 lapping. To allow overlap between adjacent groups, signals from preshower blocks
177 on the Right HRS and from both preshower and shower blocks on the Left HRS
178 were split into two identical copies using passive splitters.

179 A schematic diagram of the DAQ electronics for the Right HRS is shown in Fig. 2.
180 Preliminary electron and pion triggers were formed by passing shower (SS) and
181 preshower (PS) signals and their sums, called total shower (TS) signals, through
182 discriminators with different thresholds. For electron triggers, logical ANDs of
183 the PS discriminator and the TS discriminator outputs were used. For pions, low

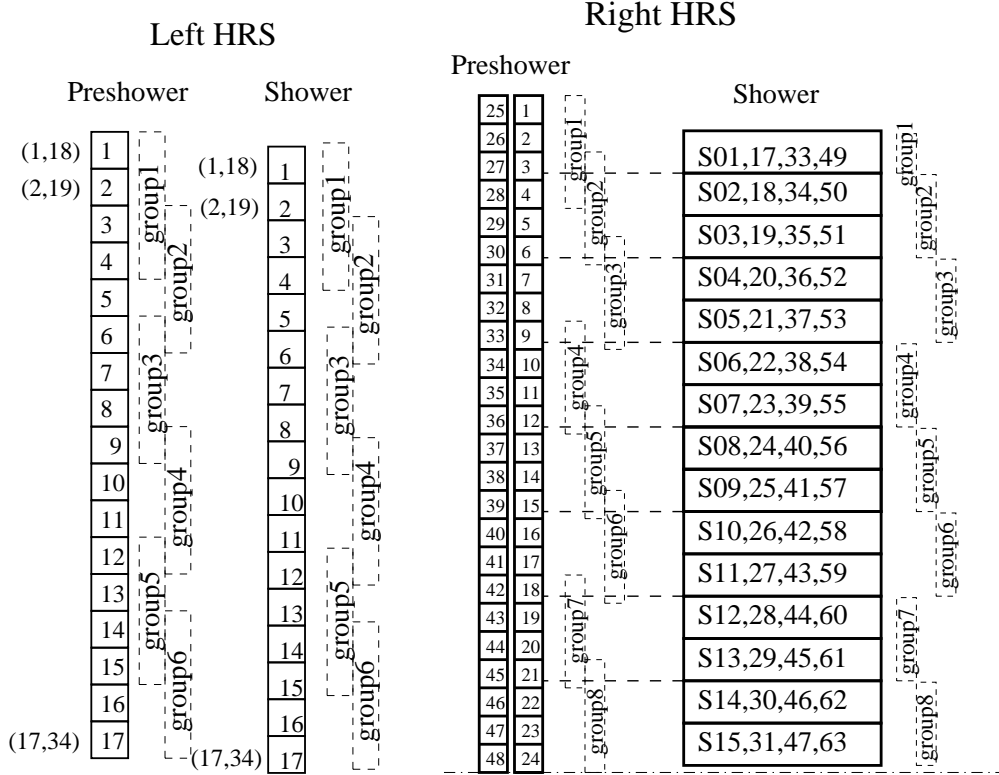


Fig. 1. Grouping scheme (side-view) for the double-layer lead-glass detectors for the Left and the Right HRS. Scattered particles enter the detector from the left. The dashed vertical bars represent the range of each group. The Right HRS Shower blocks are labeled as 1 through 64 for historical reasons, but row 16 (blocks 16, 32, 48 and 64) was not present during this experiment.

184 threshold discriminators on the TS signal alone were sent to logical OR modules
 185 to produce preliminary triggers. Additional background rejection was provided by
 186 the “GATE” circuit, which combined signals from the gas Cherenkov (GC) and the
 187 “T1” signal [6] from the scintillators (SC). Each valid coincidence between GC and
 188 T1 would produce a 150-ns wide electron GATE signal that allowed an output to be
 189 formed by the logical AND modules from the preliminary electron triggers. Each
 190 valid T1 signal without the GC signal would produce a 150-ns wide pion GATE
 191 signal that allowed an output to be formed by the logical OR modules from the
 192 preliminary pion triggers. The outputs of the logical AND and OR modules are
 193 called group electron and pion triggers, respectively. All six (eight) group electron
 194 or pion triggers were then ORed together to form the global electron or pion trigger
 195 for the Left (Right) HRS. All group and the final electron and pion triggers were
 196 counted using scalers. Because pions do not produce large enough lead-glass sig-
 197 nals to trigger the high threshold TS discriminators for the electron triggers, pions
 198 do not introduce extra counting deadtime for the electron triggers. However, the
 199 150-ns width of the electron GATE signal would cause pion contamination in the
 200 electron trigger. This effect will be presented in Section 4.

201 In order to monitor the counting deadtime of the DAQ, two identical paths of elec-

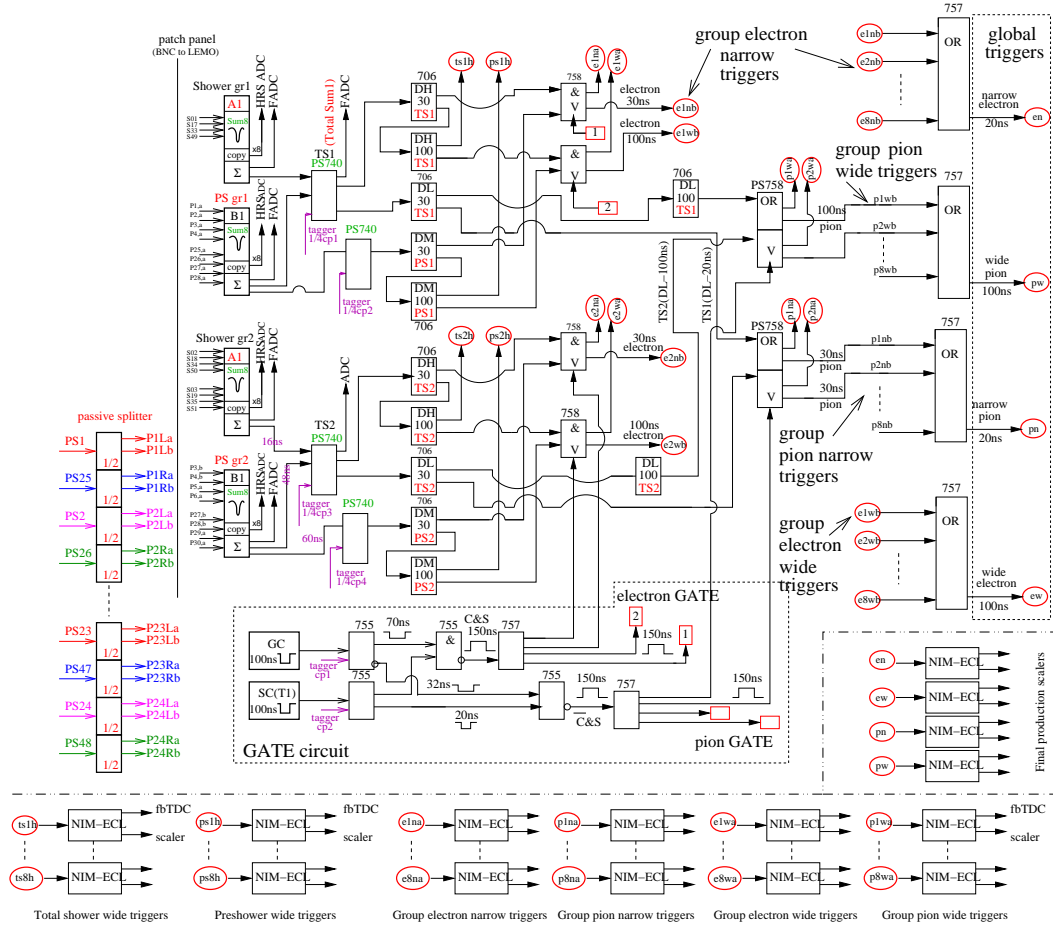


Fig. 2. [Color online] Electronics diagram for the Right HRS DAQ used by the PVDIS experiment. The Sum8's, discriminators and logic modules for two groups are shown, as well as the location of tagger signal inputs, setup of the GATE circuit using scintillator (SC) and gas Cherenkov (GC) signals, the logic units for combining triggers from all eight groups into final triggers, the counting scalers, and the monitoring fastbus TDCs. The discriminators had three different levels of threshold settings: low threshold (DL) was used on the total shower (TS) signals to form pion triggers; medium (DM) and high thresholds (DH) were used on preshower (PS) and TS signals respectively to form electron triggers. During the experiment the thresholds were approximately -20 mV for DL and DM, and in the range $(-50, -70)$ mV for DH depending on the momentum setting of the spectrometer. Electronics for the Left HRS are similar except for the grouping scheme.

202 tronics were constructed. The only difference between the two paths is in the PS
 203 and the TS discriminator output widths, set at 30 ns and 100 ns for the “narrow” and
 204 the “wide” paths, respectively. The scalers are rated for 250 MHz (4 ns deadtime)
 205 and therefore do not add to the deadtime. In addition, the output width of all logic
 206 modules was set to 15 ns, so the deadtime of the DAQ for each group is dominated
 207 by the deadtime of the discriminators. Detailed analysis of the DAQ deadtime will
 208 be presented in Section 5.

209 The SUM8 modules used for summing all lead-glass signals also served as fan-out

210 modules, providing exact copies of the input PMT signals. These copies were sent
211 to the standard HRS DAQ for calibration. During the experiment, data were col-
212 lected at low rates using reduced beam currents with both DAQs functioning, such
213 that a direct comparison of the two DAQs could be made. Vertical drift chambers
214 were used during these low rate DAQ studies. Outputs from all discriminators, sig-
215 nals from the scintillator and the gas Cherenkov, and all electron and pion group
216 and global triggers were sent to Fastbus TDCs (fbTDC) and were recorded in the
217 standard DAQ. Data from these fbTDCs were used to align the amplitude spectrum
218 and timing of all signals. They also allowed the study of the Cherenkov and the
219 lead-glass detector performance for the new DAQ.

220 Full sampling of partial analog signals was done using Flash-ADCs (FADCs) at
221 low rates intermittently during the experiment. For one group on the Left and one
222 group on the Right HRS, the preshower and the shower SUM8 outputs, the inter-
223 mediate logical signals of the DAQ, and the output electron and pion triggers were
224 recorded. These FADC data provided a study of pileup effects to confirm the dead-
225 time simulation and to provide the input parameters for the simulation, specifically
226 the rise and fall times of the signals and their widths.

227 **3 Overview of Kinematics**

228 During the experiment data were taken at two deep inelastic scattering (DIS) kine-
229 matics at $Q^2 = 1.1$ and 1.9 $(\text{GeV}/c)^2$. These were the main production kinematics
230 and will be referred to as DIS#1 and DIS#2, respectively. Due to limitation of the
231 spectrometer magnets, DIS#1 was taken only on the Left HRS, while DIS#2 was
232 taken on both Left and Right HRSs. In addition, data were taken at five kinematics
233 within or near the nucleon resonance region with their invariant mass W between
234 the $\Delta(1232)$ resonance and just above $W = 2$ GeV. These data were used for the
235 purpose of radiative corrections and will be referred to as RES I through V (al-
236 though kinematics V was located slightly above $W = 2$ GeV). Data for each of
237 the resonance settings were taken only with one HRS because of the spectrometer
238 magnet limitations as well as to optimize the beam time allocation. The kinematic
239 settings are shown in Table 1 along with the observed electron rate R_e and the pion
240 to electron ratio R_{π^-}/R_e in the HRS. The highest electron rate occurred at RES II
241 at approximately 600 kHz.

242 **4 DAQ PID Performance**

243 The PID performance of the DAQ system was studied with calibration runs taken at
244 low beam currents using fbTDC signals along with ADC data of all detector signals
245 recorded by the standard DAQ. Events that triggered the DAQ would appear as a

Kine#	HRS	E_b (GeV)	θ_0	E'_0 (GeV)	R_e (kHz)	R_{π^-}/R_e
DIS#1	Left	6.067	12.9°	3.66	≈ 210	≈ 0.5
DIS#2	Left & Right	6.067	20.0°	2.63	≈ 18	≈ 3.3
RES I	Left	4.867	12.9°	4.0	≈ 300	$< \approx 0.25$
RES II	Left	4.867	12.9°	3.55	≈ 600	$< \approx 0.25$
RES III	Right	4.867	12.9°	3.1	≈ 400	$< \approx 0.4$
RES IV	Left	6.067	15°	3.66	≈ 80	$< \approx 0.6$
RES V	Left	6.067	14°	3.66	≈ 130	$< \approx 0.7$

Table 1

Overview of kinematics settings during the experiment, including: the beam energy E_b , the spectrometer central angle setting θ_0 and central momentum setting E'_0 , the observed electron rate R_e and the π^-/e ratio R_{π^-}/R_e .

246 timing peak in the corresponding fbTDC spectrum of the standard DAQ, and a cut
 247 on this peak can be used to select those events. Figure 3 shows the preshower vs.
 248 shower signals for group 2 on the Left HRS. A comparison between no fbTDC
 249 cut and with cut on the fbTDC signal of the electron wide trigger from this group
 clearly shows the hardware PID cuts.

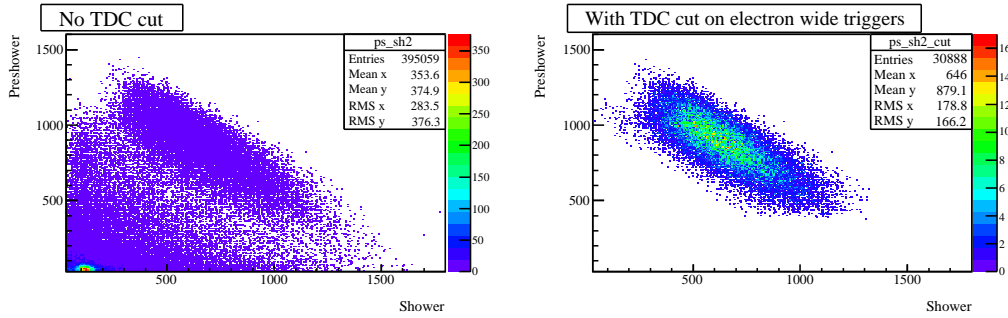


Fig. 3. Preshower vs. Shower ADC data (sum of 8 blocks each) for group 2 on the Left HRS, without the fbTDC cut (left panel) and with cut on the group 2 electron wide trigger fbTDC signal (right panel). This clearly shows the thresholds of the preshower and the total shower signals, indicating that the DAQ is selecting the correct events as electrons.

250

251 Electron efficiency and pion rejection factors of the lead-glass detector on the Left
 252 HRS during a one-hour run are shown in Fig. 4 as functions of the location of the
 253 hit of the particle in the preshower detector. PID performance on the Right HRS is
 254 similar. Electron efficiency from wide groups is slightly higher than from narrow
 255 groups because there is less event loss due to timing misalignment when taking
 256 the coincidence between the preshower and the total shower discriminator outputs.
 257 Variations in the electron efficiency across the spectrometer acceptance effectively
 258 influence the Q^2 of the measurement. For this reason, low-rate calibration data
 259 were taken daily during the experiment to monitor the DAQ PID performance, and

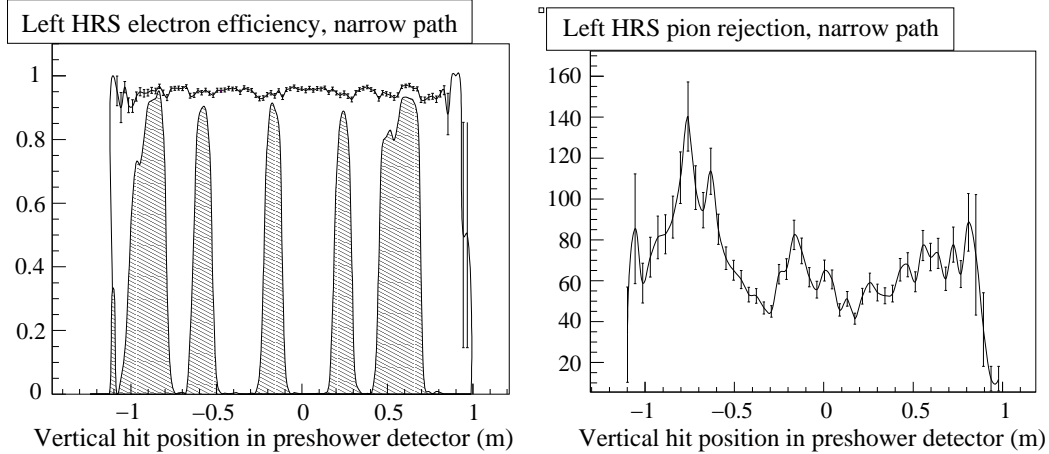


Fig. 4. Electron detection efficiency (left) and pion rejection factor (right) vs. vertical (dispersive) hit position of the particle in the preshower detector for the narrow electron triggers in the Left HRS. An 8-minute run with a reduced beam current of $2 \mu\text{A}$ at kinematics DIS #2 was used in this evaluation. For electron efficiencies, the total efficiency and the statistical error bars are shown as the curve, while the shaded area indicates events that were recorded by two adjacent groups. The average electron efficiency achieved by the lead glass detector alone for this run is $[94.60 \pm 0.11(\text{stat.})]\%$ and the average pion rejection factor is $[76.2 \pm 1.5(\text{stat.})] : 1$. PID performance for the wide path and the Right HRS are similar.

260 corrections were applied to the asymmetry data.

261 The gas Cherenkov detector signals were read out by 10 PMTs on both the Left and
 262 the Right HRS. Signals from all 10 PMTs were summed in an analog-sum module
 263 and sent to a discriminator. The discriminator output was sent to the DAQ (as shown
 264 in Fig. 2) as well as to fbTDCs. Figure 5 shows the Cherenkov ADC sum with and
 265 without the fbTDC cut, which clearly shows the capability of rejecting pions.

266 As described in the Introduction, pion contamination in the electron trigger would
 267 affect the measured electron asymmetry as $A_m = (1 - f_{\pi/e})A_e + f_{\pi/e}A_\pi$ where A_m
 268 and A_e are the measured and the true electron asymmetries, respectively, and A_π is
 269 the parity violation asymmetry of pion production. The pion contamination in the
 270 electron trigger, $f_{\pi/e}$, comes from two effects: There is a small possibility that a
 271 pion could trigger both the lead-glass and the gas Cherenkov detectors, causing a
 272 false electron trigger output. This possibility is determined by the direct combina-
 273 tion of the pion rejection factors of the two detectors and is below 10^{-4} . A larger
 274 effect comes from the width of the electron GATE signal: Since each coincidence
 275 between the gas Cherenkov and the scintillator signals would open the electron
 276 counting GATE by 150 ns, while the DAQ deadtime of the lead-glass detector is
 277 less than this value, pions that arrived after the DAQ deadtime but before the clos-
 278 ing of the electron GATE signal would cause a false electron trigger. The sum of
 279 the two effects can be written as

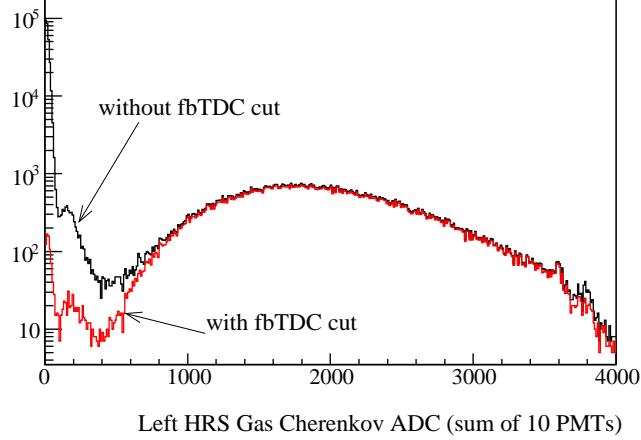


Fig. 5. [Color online] Gas Cherenkov ADC data (sum of 10 PMTs) for the Left HRS during a one-hour run at kinematics DIS #2, with a fbTDC cut on the Cherenkov discriminator output and without. The beam current during this run was about $100 \mu\text{A}$, the incident electron rate on the detector was about 23 kHz with a pion to electron rate ratio of approximately 3.5. The electron efficiency achieved by the gas Cherenkov alone for this kinematics on the Left HRS was approximately 99% with a pion rejection of approximately 300:1, see Table 2. The discriminator clearly selected electrons while rejecting pions.

$$f_{\pi/e,n(w)} = \frac{R_{\pi}\eta_{\pi}^{GC}\eta_{\pi}^{LG}}{R_e\eta_e^{GC}\eta_e^{LG}} + \frac{R_{\pi}\eta_{\pi}^{LG}\{R_e\eta_e^{GC}[150 \text{ ns} - \tau_{n(w)}]\}}{R_e\eta_e^{GC}\eta_e^{LG}} \quad (3)$$

280 where R_e and R_{π} are the input electron and the pion rates, respectively; $\eta_e^{LG(GC)}$
 281 is the electron detection efficiency of the lead-glass (gas Cherenkov) detectors, and
 282 $\eta_{\pi}^{LG(GC)}$ is the pion detection efficiency, i.e., the inverse of the rejection factor,
 283 of the lead-glass (gas Cherenkov) detector. The DAQ group deadtime of the lead-
 284 glass detector for the narrow (wide) path, $\tau_{n(w)}$, is approximately 60 ns (100-110
 285 ns) and the analysis obtaining these results will be presented in the next section.
 286 The term $R_e\eta_e^{GC}[150 \text{ ns} - \tau_{n(w)}]$ gives the probability of a pion's arriving within
 287 a valid electron GATE signal and thus such a pion can not be rejected by the gas
 288 Cherenkov detector.

289 The electron detection efficiency and pion rejection factor averaged throughout the
 290 data production period are shown in Tables 2 and 3 for DIS and resonance kine-
 291 matics, respectively, along with the resulting pion contamination $f_{\pi/e}$ evaluated
 292 separately for the narrow and the wide paths.

293 As shown in Tables 2-3, the overall pion contamination was on the order of $2 \times$
 294 10^{-4} or lower throughout the experiment. Because pions are produced from nucleon
 295 resonance decays, the parity violation asymmetry of pion production is expected to
 296 be no larger than that of scattered electrons with the same momentum. This was
 297 confirmed by asymmetries formed from pion triggers during this experiment. The
 298 uncertainty in the electron asymmetry due to pion contamination is therefore on the
 299 order of 2×10^{-4} and is negligible compared with the 3–4% statistical uncertainty.

DIS Kinematics and Spectrometer combinations			
	DIS# 1	DIS# 2	
HRS	Left	Left	Right
Electron detection efficiency η_e (%)			
GC	99.14 ± 0.02	99.03 ± 0.03	98.19 ± 0.06
LG, n	91.93 ± 0.04	94.50 ± 0.06	94.36 ± 0.04
LG, w	92.88 ± 0.04	95.79 ± 0.06	95.23 ± 0.04
GC+LG, n	91.14 ± 0.04	93.58 ± 0.06	92.65 ± 0.07
GC+LG, w	92.08 ± 0.04	94.86 ± 0.06	93.51 ± 0.07
Pion rejection $1/\eta_\pi$			
GC	158.6 ± 3.5	301.2 ± 5.2	414.3 ± 6.2
LG, n	101.5 ± 1.6	78.9 ± 0.9	72.7 ± 0.3
LG, w	103.9 ± 1.7	81.5 ± 1.0	74.3 ± 0.3
Pion contamination in the electron trigger $f_{\pi/e}$, narrow path ($\times 10^{-4}$)			
$f_{\pi/e,n}$	1.07	1.97	1.30
(stat.)	± 0.02	± 0.03	± 0.01
(syst.)	± 0.24	± 0.18	± 0.10
(total)	± 0.24	± 0.18	± 0.10
Pion contamination in the electron trigger $f_{\pi/e}$, wide path ($\times 10^{-4}$)			
$f_{\pi/e,w}$	0.72	1.64	0.92
(stat.)	± 0.01	± 0.03	± 0.01
(syst.)	± 0.22	± 0.17	± 0.13
(total)	± 0.22	± 0.17	± 0.13

Table 2

Average electron detection efficiency and pion rejection factor of electron triggers achieved for the DIS kinematics through the lead glass (LG) and the gas Cherenkov (GC) detectors, respectively, and the combined performance. The error bars of the efficiencies and the rejection factors are statistical only. The error bars for $f_{\pi/e}$, $\Delta f_{\pi/e,n(w)}$, are shown separately for statistical uncertainties, systematic uncertainties due to our understanding of the rates, detector efficiencies and deadtimes, and day-to-day variations in the measured detector efficiencies.

Resonance Kinematics and Spectrometer combinations					
	RES I	RES II	RES III	RES IV	RES V
HRS	Left	Left	Right	Left	Left
Electron detection efficiency η_e (%)					
GC	99.16 ± 0.09	99.17 ± 0.13	98.59 ± 0.11	99.41 ± 0.07	99.16 ± 0.11
LG, n	97.73 ± 0.07	97.13 ± 0.07	98.14 ± 0.06	84.71 ± 0.18	84.66 ± 0.21
LG, w	98.32 ± 0.07	97.83 ± 0.08	98.56 ± 0.06	85.31 ± 0.18	85.88 ± 0.23
GC+LG, n	96.91 ± 0.11	96.32 ± 0.15	96.76 ± 0.12	84.20 ± 0.20	83.95 ± 0.24
GC+LG, w	97.49 ± 0.11	97.02 ± 0.15	97.17 ± 0.13	84.80 ± 0.20	85.16 ± 0.26
Pion rejection $1/\eta_\pi$					
GC	82.8 ± 9.2	97.7 ± 10.5	195.0 ± 24.5	149.6 ± 10.2	151.4 ± 11.5
LG, n	43.6 ± 4.0	57.4 ± 5.4	37.0 ± 0.9	182.4 ± 15.1	207.2 ± 20.5
LG, w	39.4 ± 3.6	53.5 ± 5.1	33.9 ± 0.9	171.4 ± 14.1	201.1 ± 23.5
Pion contamination in the electron trigger $f_{\pi/e}$, narrow path ($\times 10^{-4}$)					
$f_{\pi/e,n}$	0.79	2.40	3.82	0.26	0.45
(stat.)	± 0.02	± 0.06	± 0.02	± 0.01	± 0.01
(syst.)	± 0.11	± 0.19	± 0.23	± 0.02	± 0.03
(total)	± 0.11	± 0.20	± 0.23	± 0.03	± 0.03
Pion contamination in the electron trigger $f_{\pi/e}$, wide path ($\times 10^{-4}$)					
$f_{\pi/e,w}$	0.54	1.50	2.14	0.22	0.32
(stat.)	± 0.02	± 0.04	± 0.02	± 0.01	± 0.01
(syst.)	± 0.14	± 0.25	± 0.48	± 0.03	± 0.04
(total)	± 0.15	± 0.25	± 0.48	± 0.03	± 0.04

Table 3

Average electron detection efficiency and pion rejection factor of electron triggers achieved for the resonance kinematics through the lead glass (LG) and the gas Cherenkov (GC) detectors, respectively, and the combined performance. The error bars of the efficiencies and the rejection factors are statistical only. The error bars for $f_{\pi/e}$, $\Delta f_{\pi/e,n(w)}$, are shown separately for statistical uncertainties, systematic uncertainties due to our understanding of the rates, detector efficiencies and deadtimes, and day-to-day variations in the measured detector efficiencies.

To understand fully the effect of pion background on the measured electron asymmetry, it is important to extract asymmetries of the pion background to confirm that they are indeed smaller than the electron asymmetry. A complete PID analysis was carried out on the pion triggers of the DAQ where the electron contamination in the pion trigger $f_{e/\pi}$ was evaluated in a similar method as $f_{\pi/e}$ above, following

$$f_{e/\pi,n(w)} = \frac{R_e \xi_e^{GC} \xi_e^{LG}}{R_\pi \xi_\pi^{GC} \xi_\pi^{LG}} + \frac{R_e \xi_e^{LG} \{R_\pi \xi_\pi^{GC} [150 \text{ ns} - \tau_n(w)]\}}{R_\pi \xi_\pi^{GC} \xi_\pi^{LG}} \quad (4)$$

300 where as before R_e and R_π are the electron and the pion rates incident on the de-
 301 tectors, respectively; the detection efficiencies ξ are now defined for the pion trig-
 302 gers of the DAQ: $\xi_e^{LG(GC)}$ is the electron detection efficiency of the lead-glass (gas
 303 Cherenkov) detectors, and $\xi_\pi^{LG(GC)}$ is the pion detection efficiency of the lead-glass
 304 (gas Cherenkov) detector. Although the goal of the pion triggers is to collect pions,
 305 only the gas Cherenkov played a role in rejecting electrons in the pion trigger, and
 306 all electrons would form valid pion triggers in the lead-glass counters. Therefore
 307 $\xi_e^{LG} \approx 1$ and the electron contamination is high. Results for electron contamination
 308 in the pion trigger are summarized in Tables 4 and 5.

309 5 DAQ Deadtime

310 Deadtime is the amount of time after an event during which the system is unable
 311 to record another event. Identifying the exact value of the deadtime is always a
 312 challenge in counting experiments. By having a narrow and a wide path, we can
 313 observe the trend in the deadtime: The wider path should have higher deadtime. By
 314 matching the observed trend with our simulation we can benchmark and confirm
 315 the result of our deadtime simulation. In addition, dividing lead-glass blocks into
 316 groups greatly reduces the deadtime loss in each group compared with summing
 317 all blocks together and forming only one final trigger.

318 To illustrate the importance of the deadtime, consider its effect on the asymmetry A .
 319 For a simple system with only one contribution to the deadtime loss δ , the observed
 320 asymmetry A_O is related to the true asymmetry A according to $A_O = (1 - \delta)A$. In
 321 this experiment δ was expected to be on the order of (1-2)%. Since the statistical
 322 accuracy of the asymmetry is (3-4)%, it was desirable to know δ with a (10-20)%
 323 relative accuracy so that it would become a negligible systematic error. The DAQ
 324 used in this experiment, however, was more complex and had three contributions
 325 to the deadtime as listed below:

- 326 (1) The ‘‘group’’ deadtime: deadtime due to discriminators and logical AND mod-
 327 ules used to form group triggers.
- 328 (2) The ‘‘GATE’’ deadtime: deadtime from the GATE circuit that used scintillators
 329 and gas Cherenkov signals to form the GATE signals, which controlled the

Kinematics and Spectrometer Combinations			
	DIS#1	DIS#2	
HRS	Left	Left	Right
Pion detection efficiency ξ_π (%)			
GC	99.52 ± 0.01	99.73 ± 0.01	99.74 ± 0.01
LG, n	21.67 ± 0.01	79.72 ± 0.02	15.61 ± 0.01
LG, w	21.67 ± 0.01	79.71 ± 0.02	15.60 ± 0.01
GC+LG, n	21.57 ± 0.01	79.70 ± 0.02	15.57 ± 0.01
GC+LG, w	21.57 ± 0.01	79.69 ± 0.02	15.56 ± 0.01
Electron rejection $1/\xi_e$			
GC	31.42 ± 0.78	89.44 ± 2.48	48.48 ± 1.55
LG, n	1.0468 ± 0.0003	1.0487 ± 0.0005	1.0271 ± 0.0002
LG, w	1.0469 ± 0.0003	1.0499 ± 0.0005	1.0279 ± 0.0002
Electron contamination in pion triggers $f_{e/\pi}$, narrow path			
$f_{e/\pi,n}$	0.2653	0.0331	0.0103
(stat.)	± 0.0029	± 0.0006	± 0.0002
(syst.)	± 0.0602	± 0.0033	± 0.0013
(total)	± 0.0603	± 0.0034	± 0.0013
Electron contamination in pion triggers $f_{e/\pi}$, wide path			
$f_{e/\pi,w}$	0.2176	0.0281	0.0091
(stat.)	± 0.0029	± 0.0006	± 0.0002
(syst.)	± 0.0573	± 0.0036	± 0.0012
(total)	± 0.0573	± 0.0037	± 0.0013

Table 4

Average pion detection efficiency and electron rejection factor of pion triggers achieved for DIS kinematics through the lead glass (LG) and the gas Cherenkov (GC) detectors, respectively, and the combined performance. The error bars of the efficiencies and the rejection factors are statistical only. The error bars for $f_{e/\pi}$, $\Delta f_{e/\pi,n(w)}$, are shown separately for statistical uncertainties, systematic uncertainties, and day-to-day variations in the measured detector efficiencies.

Kinematics and Spectrometer Combinations					
	RES I	RES II	RES III	RES IV	RES V
HRS	Left	Left	Right	Left	Left
Pion detection efficiency ξ_π (%)					
GC	98.82 ± 0.13	98.96 ± 0.11	99.43 ± 0.07	99.38 ± 0.04	99.47 ± 0.04
LG, n	26.27 ± 0.62	25.65 ± 0.55	82.78 ± 0.16	21.16 ± 0.25	20.69 ± 0.28
LG, w	27.07 ± 0.65	26.14 ± 0.57	83.60 ± 0.17	22.54 ± 0.26	20.71 ± 0.28
GC+LG, n	25.96 ± 0.64	25.39 ± 0.56	82.31 ± 0.17	21.03 ± 0.25	20.58 ± 0.28
GC+LG, w	26.75 ± 0.66	25.87 ± 0.58	83.12 ± 0.18	22.40 ± 0.26	20.60 ± 0.28
Electron rejection $1/\xi_e$					
GC	121.36 ± 21.71	118.33 ± 34.02	72.91 ± 5.67	101.43 ± 16.59	74.80 ± 13.57
LG, n	1.0167 ± 0.0006	1.0194 ± 0.0006	1.0114 ± 0.0005	1.0677 ± 0.0014	1.0652 ± 0.0016
LG, w	1.0167 ± 0.0006	1.0105 ± 0.0006	1.0064 ± 0.0005	1.0344 ± 0.0013	1.0541 ± 0.0016
Electron contamination in pion triggers $f_{e/\pi}$, narrow path					
$f_{e/\pi,n}$	0.4114	0.3155	0.0849	0.1852	0.1871
(stat.)	± 0.0117	± 0.0061	± 0.0006	± 0.0062	± 0.0058
(syst.)	± 0.0163	± 0.0151	± 0.0029	± 0.0038	± 0.0050
(total)	± 0.0201	± 0.0163	± 0.0030	± 0.0073	± 0.0077
Electron contamination in pion triggers $f_{e/\pi}$, wide path					
$f_{e/\pi,w}$	0.3423	0.2409	0.0633	0.1661	0.1598
(stat.)	± 0.0116	± 0.0062	± 0.0006	± 0.0063	± 0.0057
(syst.)	± 0.0200	± 0.0190	± 0.0059	± 0.0049	± 0.0064
(total)	± 0.0231	± 0.0200	± 0.0060	± 0.0080	± 0.0086

Table 5

Average pion detection efficiency and electron rejection factor of pion triggers achieved for resonance kinematics through the lead glass (LG) and the gas Cherenkov (GC) detectors, respectively, and the combined performance. The error bars of the efficiencies and the rejection factors are statistical only. The error bars for $f_{e/\pi}$, $\Delta f_{e/\pi,n(w)}$, are shown separately for statistical uncertainties, systematic uncertainties, and day-to-day variations in the measured detector efficiencies.

330 AND (OR) module of each group to form group electron (pion) triggers.
 331 (3) The “OR” deadtime: deadtime due to the logical OR module used to combine
 332 all group triggers into final global triggers.

333 The total deadtime is a combination of all three. In order to evaluate the DAQ
 334 deadtime, a full-scale trigger simulation is necessary. This trigger simulation will
 335 be described in the next section followed by results on the group, GATE, and OR
 336 deadtime as well as on the total deadtime correction that was applied to the asym-
 337 metry data.

338 5.1 Trigger Simulation

339 The Hall A Trigger Simulation (HATS) was developed for the purpose of dead-
 340 time study for this experiment. The inputs to HATS include the analog signals for
 341 preshower, shower, scintillator and gas Cherenkov. The signal amplitudes were pro-
 342 vided by ADC data from low-current runs, and the signal rates were from high-
 343 current production runs. The rise and fall times for the preshower and shower
 344 SUM8 outputs play an important role in HATS. The signal shape is simulated by
 345 the function $S(t) = Ate^{-t/\tau}$, where A is related to the amplitude of the signal, and
 346 the time constant τ was determined from FADC data, see Fig. 6.

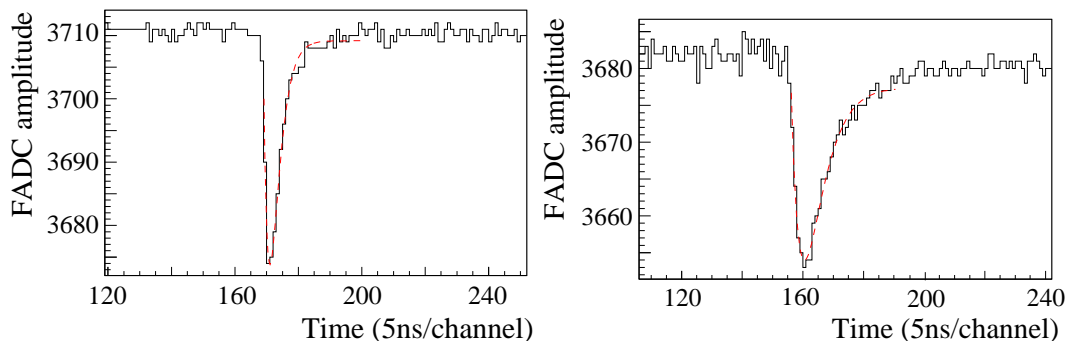


Fig. 6. [Color online] Calibration of time constants τ for Preshower (left) and Shower (right) of the Right HRS. The FADC snapshots (histograms) is compared with the fit $S(t) = Ate^{-t/\tau}$ (smooth dashed curves). The time constant τ was found to be approximately 11 ns for the Right HRS Preshower, and 21 – 22 ns for the Left HRS Preshower and Shower as well as for the Right HRS Shower.

347 With the recorded DAQ electronics and delay cables, HATS first rebuilds the DAQ
 348 system on the software level. At each nano-second, detector input signals are gen-
 349 erated randomly according to the actual event rates and signal shape, and HATS
 350 simulates output signals from all discriminators, AND, and OR modules. Figure 7
 351 shows a fraction of the DAQ electronics and the simulated results for a very short
 352 time period. By comparing output with input signals, HATS provides results on the
 353 fractional loss due to deadtime for all group and global triggers with respect to the
 354 input signal.

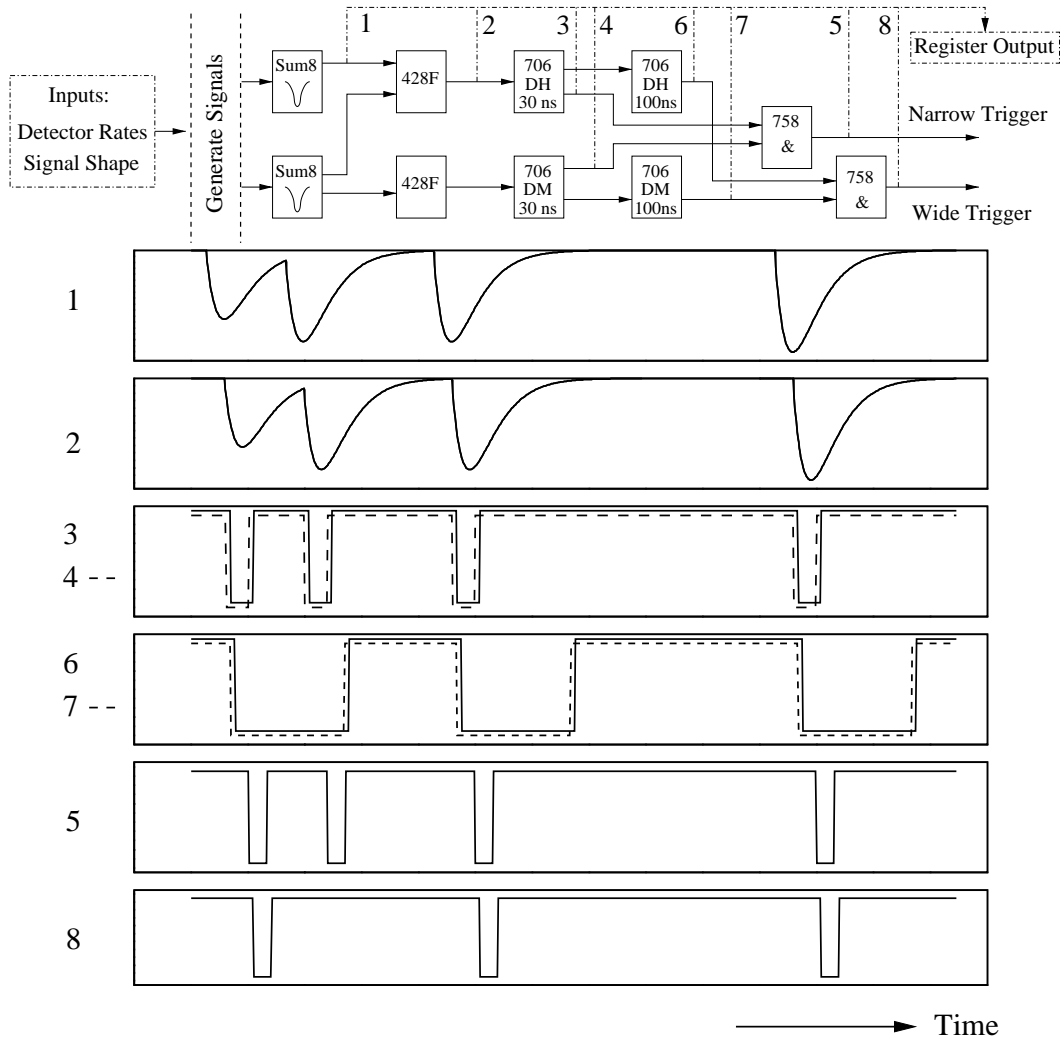


Fig. 7. Top: A fraction of the group electron trigger. Each point corresponds to: 1 – Shower sum of the group; 2 – Total shower sum of the group; 3 – Total shower discriminator output (high threshold), narrow path; 4 – Preshower discriminator output (medium threshold), narrow path; 5 – group electron trigger, narrow path; 6 – Total shower discriminator output, wide path; 7 – Preshower discriminator output, wide path; 8 – group electron trigger, wide path. Bottom: Signals 1-8 as simulated by HATS. One can see that the second physical event is recorded by the narrow path group trigger (5) but not the wide path (8) due to deadtime loss.

355 5.2 Group Deadtime Measurement

356 In order to study the group deadtime, a high rate pulser signal (“tagger”) was mixed
 357 with the Cherenkov and all preshower and total shower signals using analog sum-
 358 ming modules, see Figs. 2 and 8. In the absence of all detector signals, a tagger
 359 pulse produces without loss an electron trigger output and a “tagger-trigger coinci-
 360 dence” pulse between this output and the “delayed tagger” – the tagger itself with
 361 an appropriate delay to account for the DAQ response time. When high-rate detec-

362 tor signals are present, however, some of the tagger pulses would not be able to
 363 trigger the DAQ due to deadtime. The deadtime loss in the electron trigger output
 364 with respect to the tagger input has two components:

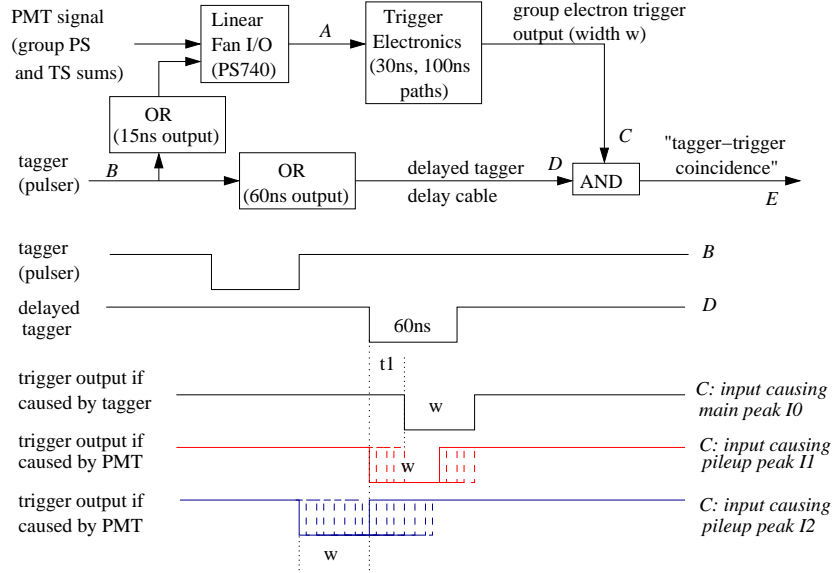
- 365 (1) The count loss R_o/R_i : When a detector PMT signal precedes the tagger signal
 366 by a time interval δt shorter than the DAQ deadtime but longer than $w + t_1$,
 367 the tagger signal is lost and no coincidence output is formed. Here w is the
 368 width of the electron trigger output and t_1 is the time interval by which the
 369 delayed tagger precedes the tagger's own trigger output, see Fig. 8. During
 370 the experiment w was set to 15 ns for all groups, and t_1 was measured at the
 371 end of the experiment and found to be between 20 and 40 ns for all narrow
 372 and wide groups of the two HRSs.
- 373 (2) The pileup fraction p : When a PMT signal precedes the tagger signal by a time
 374 interval δt shorter than $w + t_1$, there would be a coincidence output between
 375 the delayed tagger and the electron output triggered by the detector PMT sig-
 376 nal. If furthermore δt is less than the DAQ deadtime (which is possible for
 377 this experiment since the deadtime is expected to be as long as 100 ns for
 378 the wide path), the tagger itself is lost due to deadtime, and the tagger-trigger
 379 coincidence is a false count and should be subtracted. In the case where δt
 380 is shorter than $w + t_1$ but longer than the DAQ deadtime (not possible for
 381 this experiment but could happen in general), the tagger itself also triggers a
 382 tagger-trigger coincidence, but in this case, there are two tagger-trigger coin-
 383 cidence events. Both are recorded by the fbTDC if working in the multi-hit
 384 mode, and one is a false count and should be subtracted.

385 The pileup effect can be measured using the delay between the tagger-
 386 trigger coincidence output and the input tagger. This is illustrated in Fig. 8 and
 387 the pileup effect contributes to both I_1 and I_2 regions of the fbTDC spectrum.
 388 The I_1 distribution is produced by PMT pulses that arrive after the delayed
 389 tagger signal but before the tagger signal would propagate through the trig-
 390 ger electronics. Peak I_2 occurs when a PMT pulse arrives at the coincidence
 391 module earlier than the delayed tagger signal but which forms a coincidence
 392 with the delayed tagger signal, giving an output whose time is set by the lat-
 393 ter. Fractions of I_1 and I_2 relative to I_0 are expected to be $I_1/I_0 = Rt_1$ and
 394 $I_2/I_0 = Rw$, respectively, where R is the PMT signal rate. The pileup effect
 395 was measured using fbTDC spectrum for electron narrow and wide triggers
 396 for all groups. Data for $I_{1,2}$ extracted from fbTDC agree very well with the
 397 expected values.

The relative loss of tagger events due to DAQ deadtime is evaluated as

$$D = 1 - (1 - p)(R_o/R_i), \quad (5)$$

398 where R_i is the input tagger rate, R_o is the output tagger-trigger coincidence rate,
 399 and $p = (I_1 + I_2)/I_0$ is a correction factor for pileup effects as defined in Fig. 8.
 400 Results for the deadtime loss D are shown in Figs. 9 and 10, for group 4 on the left



from tagger events

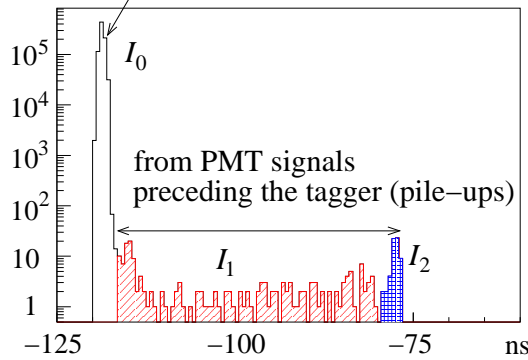


Fig. 8. [Color online] Top: schematic diagram for the tagger setup and signal timing sequence. The two logical OR units immediately following the tagger input “B” serve as width adjusters. Bottom: fbTDC spectrum for the relative timing between tagger-trigger coincidence and the input tagger. The fbTDC module worked in a common stop and the multi-hit mode. Two different scenarios are shown: 1) Main peak I_0 (hollow peak): when there is no PMT signal preceding the tagger, the tagger triggers the DAQ and forms a tagger-trigger coincidence. 2) Pileup events I_1 (light-shaded region) and I_2 (heavy-shaded region): when there is a PMT signal preceding the tagger by a time interval shorter than $w + t_1$, the PMT signal triggers the DAQ and forms a tagger-trigger coincidence signal with the delayed tagger.

401 HRS and group 4 on the right HRS, respectively, and are compared with simula-
 402 tion. Different beam currents between 20 and 100 μA were used in this dedicated
 403 deadtime measurement. In order to reduce the statistical fluctuation caused by the
 404 limited number of trials in the simulation within a realistic computing time, simu-
 405 lations were done at higher rates than the actual measurement.

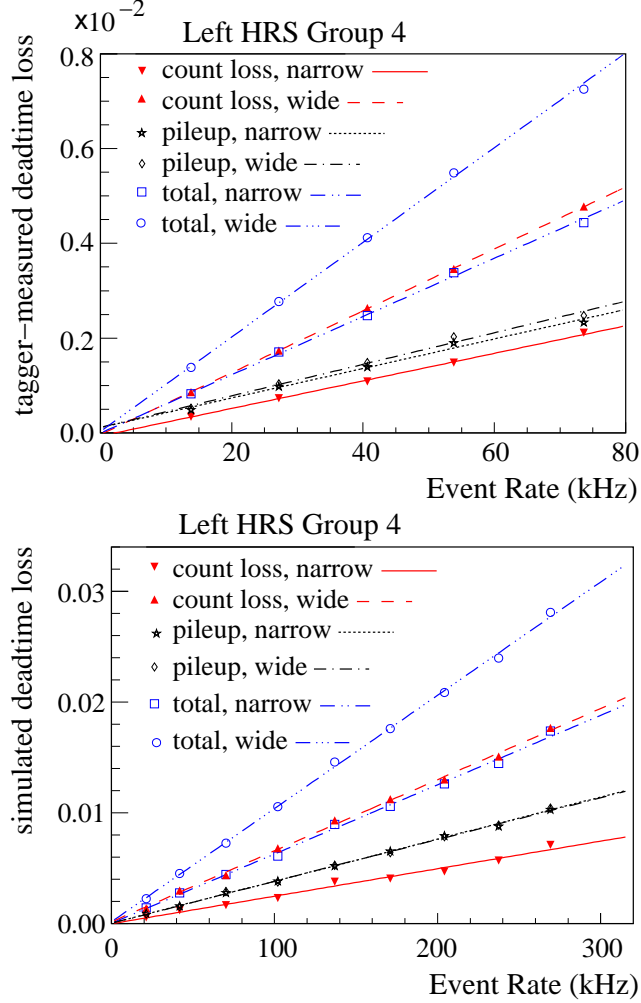


Fig. 9. [Color online] Deadtime loss vs. event rate from the tagger method for group 4 on the Left HRS. Top: actual deadtime loss from tagger measurements; Bottom: simulated deadtime loss of the tagger. The tagger fractional count loss $1 - R_o/R_i$ (fit by solid and dashed lines) and the pileup correction p (fit by dotted and dash-dotted lines) are combined to form the total group deadtime D (fit by dash-double-dotted and dash-triple-dotted lines). These data were taken (or simulated) at kinematics DIS #1. To minimize the statistical uncertainty while keeping the computing time reasonable, the simulation used higher event rates than the tagger measurement. The total group deadtime can be determined from the linear fit slope coefficients: tagger data narrow $(61.5 \pm 0.2) \times 10^{-9}$ s, wide $(99.9 \pm 0.3) \times 10^{-9}$ s, simulation narrow $(62.5 \pm 1.4) \times 10^{-9}$ s, wide $(102 \pm 1.3) \times 10^{-9}$ s. Group 4 is from the central blocks of the lead-glass detector and has the highest rate among all groups.

406 The slope of the tagger loss vs. event rate, as shown in Figs. 9 and 10, gives the
 407 value of group deadtime in seconds. One can see that the deadtime for the wide path
 408 is approximately 100 ns as expected. The deadtime for the narrow path, on the other
 409 hand, is dominated by the input PMT signal width (typically 60-80 ns) instead of
 410 the 30-ns discriminator width. The simulated group deadtime agrees with the data
 411 at a 10% level or better, for both HRSs and for both wide and narrow paths.

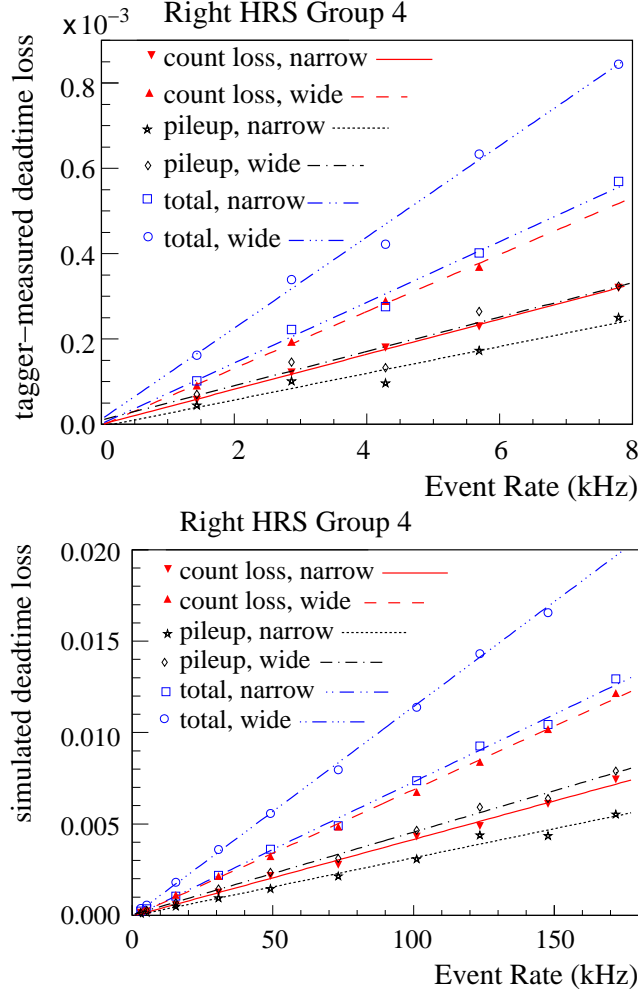


Fig. 10. [Color online] Deadtime loss vs. group event rate from the tagger method for group 4 on the Right HRS. Top: tagger data; Bottom: simulation. These data were taken (or simulated) at kinematics DIS #2. The total group deadtime can be determined from the linear fit slope coefficients: tagger data narrow $(71.1 \pm 0.9) \times 10^{-9}$ s, wide $(107 \pm 1.2) \times 10^{-9}$ s, simulation narrow $(73.9 \pm 1.5) \times 10^{-9}$ s, wide $(115 \pm 1.5) \times 10^{-9}$ s. Group 4 is from the central blocks of the lead-glass detector and has the highest rate among all groups. See Fig. 9 caption for more details.

412 The above tagger measurements were performed at kinematics DIS#1 on the Left
 413 and DIS#2 on the Right HRS. No tagger data was available for resonance kine-
 414 matics. However since the group deadtime is expected to rely only on the signal
 415 width and the module width settings, as demonstrated by the tagger data, a 10%
 416 systematic uncertainty was used for group deadtime for all kinematics.

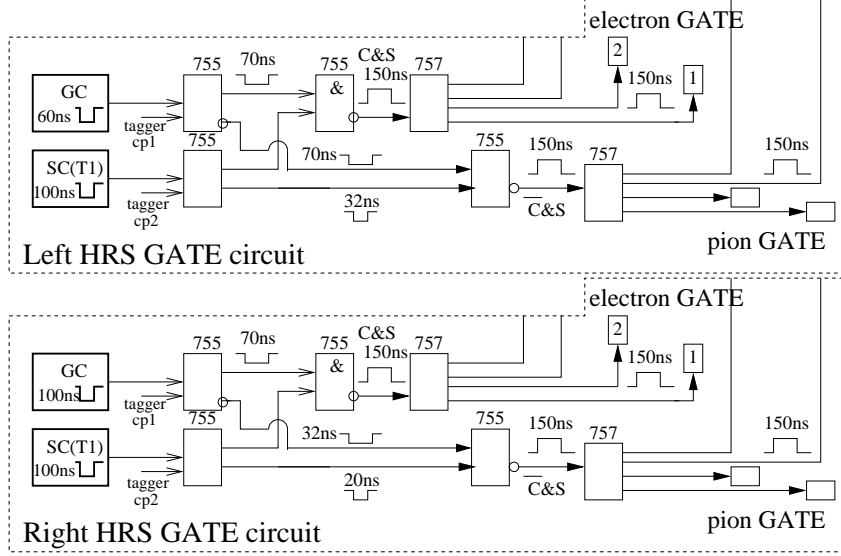


Fig. 11. A zoom-in view of the GATE electronics for Left (top) and Right (bottom) spectrometers.

417 5.3 Gate Deadtime Evaluation

418 Figure 11 shows the GATE electronics for both spectrometers, with the bottom
 419 panel reproducing the GATE portion of Fig. 2. It contributes to the total deadtime
 420 as follows: When both the gas Cherenkov and the Scintillator are triggered by elec-
 421 trons, the two signals align in time and produce an electron GATE signal. However
 422 the Scintillator can be triggered by pions and other backgrounds, most of which do
 423 not trigger the Cherenkov. If an electron event arrives shortly after such background
 424 events, it triggers the Cherenkov but may not trigger the PS755 module that first
 425 processes the Scintillator signal because of the non-updating feature of PS755. In
 426 this case, the Cherenkov signal triggered by the electron may miss the Scintillator
 427 signal from the previous pion or background event and will not produce a valid
 428 electron GATE signal. Likewise, if a background event triggers the Cherenkov but
 429 not the Scintillator, it would also cause a loss to the electron events that follow
 430 shortly after. The fractional loss due to GATE deadtime can be estimated as

$$DT_{\text{gate}} = R_{SC\&GC}(w_{SC,in} - w_{SC,out}) + R_{GC\&SC}(w_{GC,in} - w_{GC,out}), \quad (6)$$

431 where $R_{SC\&GC}$ ($R_{GC\&SC}$) refers to the rate of events that triggered the Scintillator
 432 (Cherenkov) but not the Cherenkov (Scintillator), $w_{SC,in(out)}$ and $w_{GC,in(out)}$ refer
 433 to the input (output) signal widths of the PS755 module that first processes the
 434 Scintillator and the Cherenkov signals in the GATE electronics, respectively. Note
 435 that if the electronics used to generate the Scintillator and the Cherenkov signals
 436 have intrinsic deadtimes themselves that are longer than $w_{SC,in}$ and $w_{GC,in}$, these
 437 intrinsic deadtimes should be used in place of the measured $w_{SC,in}$ and $w_{GC,in}$.
 438 In Eq. (6), each term on the right hand side is present only if $w_{in} > w_{out}$. From

439 Fig. 11, the signal widths were measured to be: $w_{SC,in,left} = w_{SC,in,Right} = 100$ ns,
 440 $w_{SC,out,left} = w_{SC,out,Right} = 32$ ns, $w_{GC,in,left} = 60$ ns, $w_{GC,in,Right} = 100$ ns,
 441 $w_{GC,out,left} = w_{GC,out,Right} = 70$ ns. However it was observed from the data that the
 442 Left HRS Cherenkov signal had an intrinsic deadtime of longer than 70 ns. In fact,
 443 data showed both HRSs had contributions from the two terms on the right hand side
 444 of Eq. (6).

445 Because trigger rates from Scintillator and the gas Cherenkov were much higher
 446 than individual group rates, the GATE deadtime could dominate the total deadtime
 447 of the DAQ, and the difference in total deadtime loss between narrow and wide
 448 paths could be smaller than that in their group deadtimes.

449 The GATE deadtime can be extracted from the trigger simulation HATS using the
 450 known signal widths and module settings, and be compared with the estimation of
 451 Eq. (6). In addition, evidence of the GATE deadtime can be extracted from FADC
 452 data. Figure 12 shows spectra of the timing difference between the gas Cherenkov
 453 (GC) and the Scintillator (SC) signals extracted from FADC data. Timing of the
 454 GC signal should represent the timing of an electron event, while the SC signal can
 455 be triggered by the same electron (as represented by the main peak near 0 ns), or
 456 a pion event that preceded the electron (as represented by the region < 0 ns). The
 457 region beyond ± 100 ns were pure random events since the SC signal input to the
 458 GATE electronics was only 100 ns wide. As one can see, the region between -100
 459 and ≈ -30 ns represents a “dead zone” where the preceding pion triggered the
 460 PS755 unit that first processed the SC signal, and caused the electron events that
 461 followed to not trigger the GATE circuit. The probability for the electron events to
 462 not be recorded by the DAQ due to this GATE deadtime is thus the ratio of the dead
 463 zone area (N_1) and the area of the main peak near 0 ns (N_0), see Fig. 12.

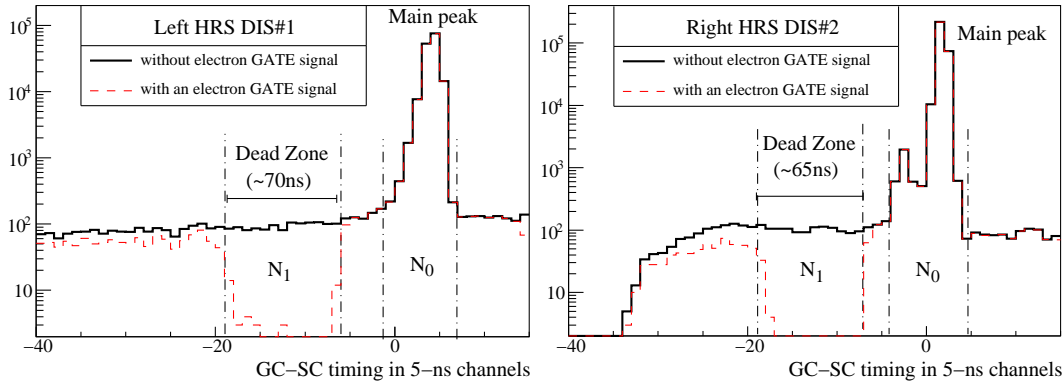


Fig. 12. [Color online] Timing difference between Gas Cherenkov and Scintillator signals in 5-ns channels. These data were taken with a beam current of $110 \mu A$ and at kinematics DIS#1 on the Left and DIS#2 on the Right HRS, respectively. The fractional loss of electron events due to GATE deadtime can be estimated using the ratio of N_1/N_0 , where N_1 is the count difference between the two spectra in the dead zone, and N_0 is the counts under the main peak near 0 ns. See text for details.

464 Figure 13 shows comparisons of the fractional losses due to GATE deadtime es-

465 timated using trigger simulation, the analytic method Eq. (6), and FADC data ex-
 466 tracted from Fig. 12. The agreement between simulation and FADC was found to
 467 be better than 10% and this was used as the systematic uncertainty of the GATE
 468 deadtime. For resonance kinematics no FADC data was available. GATE deadtime
 469 for resonance data was obtained from trigger simulation and the same systematic
 470 uncertainty was used because the mechanism of the GATE deadtime was expected
 471 to remain the same throughout the experiment.

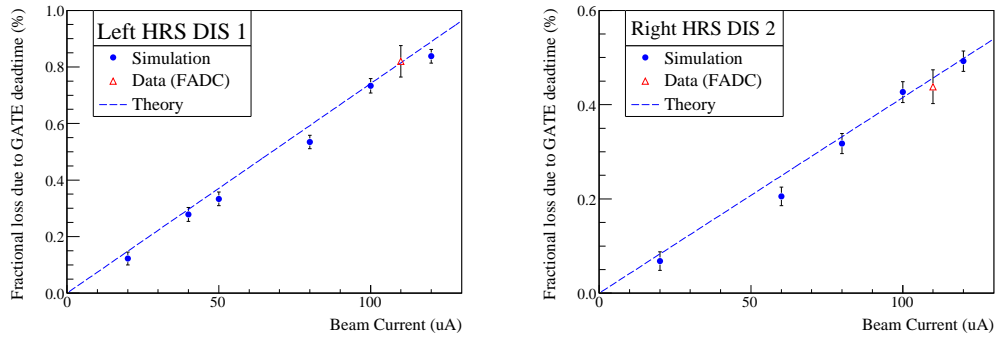


Fig. 13. [Color online] Fractional loss due to GATE deadtime as a function of beam current obtained from trigger simulation (solid circles), the analytic method Eq. (6) (dashed line), and FADC data (open triangle). Error bars for simulations are statistical.

472 5.4 OR Deadtime Evaluation

473 There is no direct measurement of the logical OR deadtime, but the effect of the
 474 logical OR module is straightforward and can be calculated analytically: When
 475 two electron triggers from different groups overlap in time as they arrive at the
 476 logical OR module, they generate only one output in the global trigger. This OR
 477 deadtime loss can be calculated using the recorded trigger rates and the known
 478 trigger signal widths. To confirm the analytic method results, the OR deadtime was
 479 evaluated from trigger simulation by subtracting the group and the GATE deadtimes
 480 from the total deadtime, all three of which were direct results from the simulation.
 481 The difference between the analytic method and trigger simulation was used as the
 482 systematic uncertainty of the OR deadtime.

483 5.5 Total Deadtime Evaluation

484 The simulated deadtime loss of the global electron triggers and its decomposition
 485 into group, GATE, and OR are shown in Table 6, along with the total deadtime
 486 correction at a beam current of 100 μ A. The total deadtime loss not only increases
 487 with higher electron rate R_e , but also with higher pion to electron ratio R_π/R_e
 488 (see Table 1) which would cause larger GATE deadtime. The deadtime loss is also
 489 shown in Fig. 14 as a function of the total event rate.

Table 6

Simulated DAQ deadtime loss in percent for all kinematics and for both narrow (n) and wide (w) paths, along with the fractional contributions from group, GATE, and OR dead-times. The fractional deadtime from OR was calculated as one minus those from group and GATE, and its uncertainty was estimated from the difference between simulation and the analytical results. The variation of group deadtime contribution among kinematics is due to changes in the rate distribution among different groups. The uncertainty of the total deadtime is the uncertainties from group, GATE and OR added in quadrature.

Kine, HRS	Path	fractional contribution			Total deadtime loss at $100\mu\text{A}$
		Group	GATE	OR	
DIS#1, Left	n	$(20.6 \pm 2.1)\%$	$(51.3 \pm 3.5)\%$	$(28.1 \pm 4.7)\%$	$(1.45 \pm 0.09)\%$
	w	$(29.5 \pm 2.4)\%$	$(45.3 \pm 3.1)\%$	$(25.3 \pm 4.6)\%$	$(1.64 \pm 0.10)\%$
DIS#2, Left	n	$(5.4 \pm 0.8)\%$	$(81.1 \pm 5.5)\%$	$(13.5 \pm 7.0)\%$	$(0.50 \pm 0.04)\%$
	w	$(8.4 \pm 0.4)\%$	$(77.3 \pm 5.3)\%$	$(14.3 \pm 8.0)\%$	$(0.52 \pm 0.05)\%$
DIS#2, Right	n	$(4.6 \pm 0.4)\%$	$(72.9 \pm 6.0)\%$	$(22.6 \pm 17.4)\%$	$(0.57 \pm 0.10)\%$
	w	$(6.9 \pm 0.7)\%$	$(71.0 \pm 5.8)\%$	$(22.1 \pm 17.9)\%$	$(0.58 \pm 0.11)\%$
RES I, Left	n	$(26.3 \pm 3.8)\%$	$(39.3 \pm 2.7)\%$	$(34.4 \pm 1.8)\%$	$(1.45 \pm 0.07)\%$
	w	$(37.2 \pm 2.1)\%$	$(34.3 \pm 2.3)\%$	$(28.5 \pm 3.1)\%$	$(1.66 \pm 0.07)\%$
RES II, Left	n	$(27.6 \pm 4.3)\%$	$(38.8 \pm 2.7)\%$	$(33.6 \pm 7.5)\%$	$(2.19 \pm 0.20)\%$
	w	$(38.3 \pm 1.9)\%$	$(33.2 \pm 2.3)\%$	$(28.5 \pm 7.0)\%$	$(2.56 \pm 0.19)\%$
RES III, Right	n	$(22.9 \pm 1.8)\%$	$(60.0 \pm 4.9)\%$	$(17.1 \pm 18.48)\%$	$(1.96 \pm 0.38)\%$
	w	$(30.8 \pm 3.1)\%$	$(51.8 \pm 4.3)\%$	$(17.4 \pm 12.73)\%$	$(2.27 \pm 0.31)\%$
RES IV, Left	n	$(14.5 \pm 1.9)\%$	$(63.7 \pm 4.4)\%$	$(21.9 \pm 3.0)\%$	$(0.75 \pm 0.04)\%$
	w	$(21.5 \pm 1.0)\%$	$(58.2 \pm 4.0)\%$	$(20.3 \pm 2.9)\%$	$(0.82 \pm 0.04)\%$
RES V, Left	n	$(15.5 \pm 2.1)\%$	$(68.3 \pm 4.7)\%$	$(16.2 \pm 5.7)\%$	$(1.03 \pm 0.08)\%$
	w	$(22.7 \pm 1.1)\%$	$(61.7 \pm 4.2)\%$	$(15.6 \pm 3.0)\%$	$(1.14 \pm 0.06)\%$

490 Results shown in Table 6 provide a direct correction to the measured asymmetry,
491 and the uncertainties are small compared with other dominant systematic uncertain-
492 ties such as the approximately 2% uncertainty from beam polarizations. In practice,
493 the deadtime correction was applied to data on a run-by-run basis with the deadtime
494 of each run calculated using the actual beam current during the run and the linear
495 fitting results from Fig. 14.

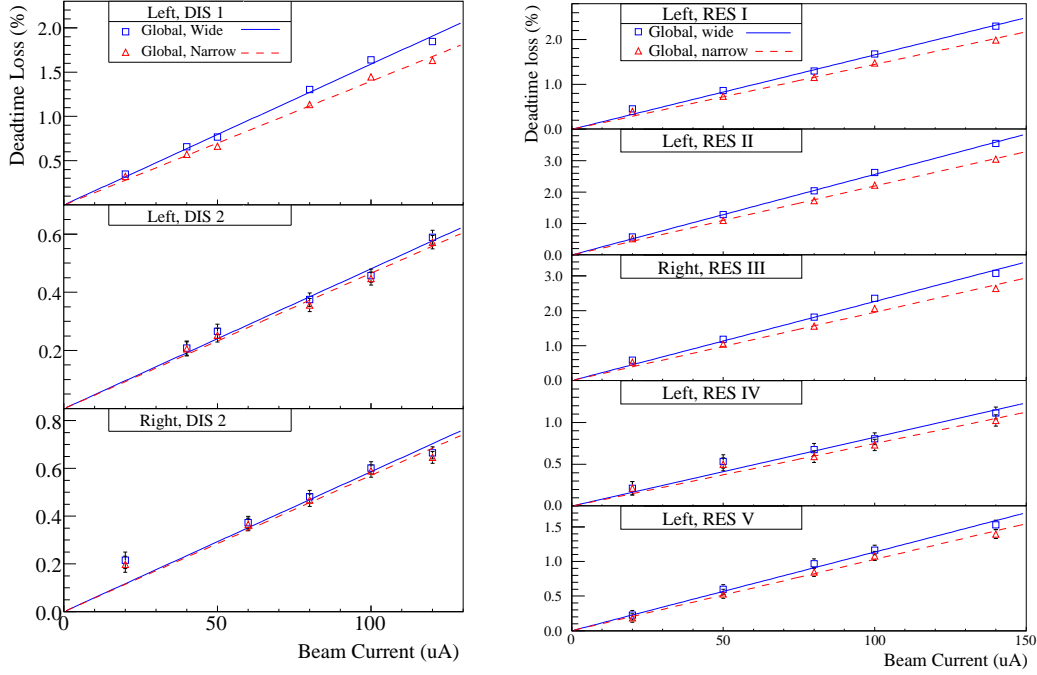


Fig. 14. [Color online] Simulated deadtime loss of the global electron trigger for the three DIS spectrometer and kinematics combinations and the five resonance kinematics, for the narrow path (open triangles, fit by dashed lines) and the wide path (open squares, fit by solid lines). The error bars shown are due to statistical uncertainty of the simulation. See Table 6 for final uncertainty evaluation of the total deadtime loss.

496 5.6 Asymmetry Measurement

497 The physics asymmetries sought for in this experiment were expected to be in the
 498 order of 10^2 ppm. The measured asymmetries were about 90% of the expected
 499 values due to beam polarization. To understand the systematics of the asymmetry
 500 measurement, a half-wave plate (HWP) was inserted in the beamline to flip the laser
 501 helicity in the polarized source during half of the data taking period. The measured
 502 asymmetries flipped sign for each beam HWP change and the magnitude of the
 503 asymmetry remained consistent within statistical error bars.

504 The asymmetries can be formed from event counts of each beam helicity pair, with
 505 33-ms of helicity right and 33-ms of helicity left beam, normalized by the beam
 506 charge. Figure 15 shows the pull distribution of these pair-wise asymmetries with
 507 the “pull” defined as

$$p_i \equiv (A_i - \langle A \rangle) / \delta A_i, \quad (7)$$

508 where A_i is the asymmetry extracted from the i -th beam helicity pair with the HWP
 509 states already corrected and $\delta A_i = 1/\sqrt{N_i^R + N_i^L}$ its statistical uncertainty with

510 $N_i^{R(L)}$ the event count from the right (left) helicity pulse of the pair, and $\langle A \rangle$ is the
 511 asymmetry averaged over all beam pairs. One can see that the asymmetry spectrum
 512 agrees to five orders of magnitude with the Gaussian distribution, as expected from
 513 purely statistical fluctuations.

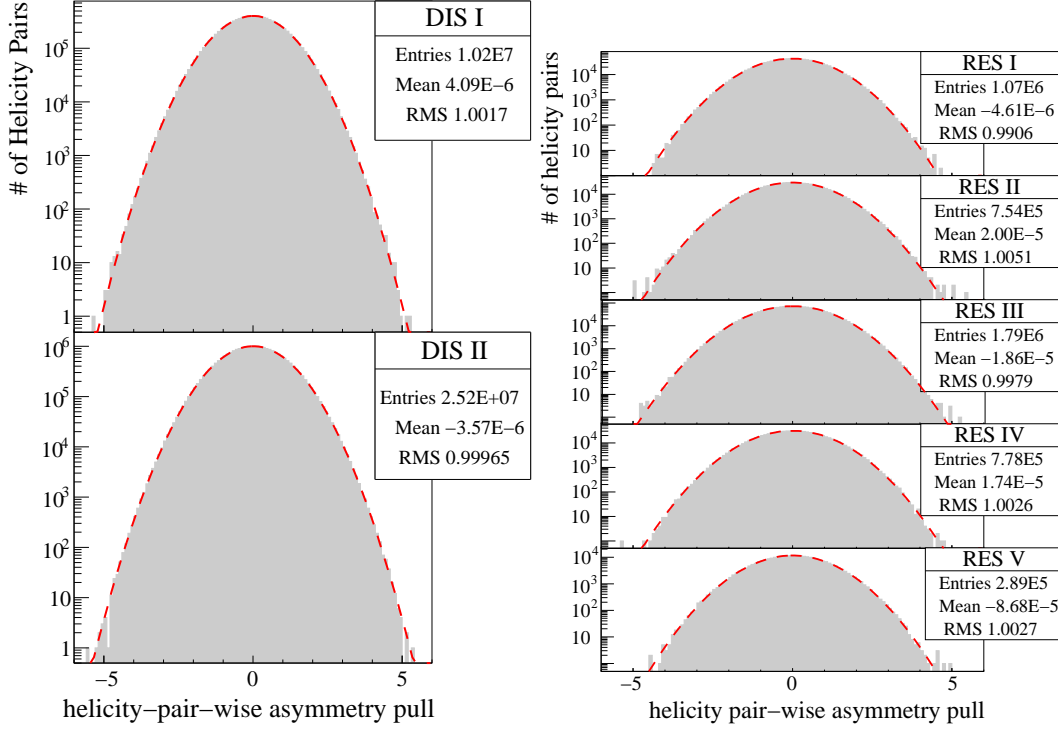


Fig. 15. [Color online] Pull distribution [Eq.(7)] for the global electron narrow trigger for the three DIS spectrometer and kinematics combinations, and the five resonance kinematics. The DIS#2 distribution has both the Left and the Right HRS data combined.

514 6 Summary

515 A scaler-based counting DAQ with hardware-based particle identification was suc-
 516 cessfully implemented in the 6 GeV PVDIS experiment at Jefferson Lab to mea-
 517 sure parity-violating asymmetries at the 10^{-4} level at event rates of up to 600 kHz.
 518 Asymmetries measured by the DAQ followed Gaussian distributions as expected
 519 from purely statistical measurements. Particle identification performance of the
 520 DAQ was measured and corrections were applied to the data on a day-to-day basis.
 521 The overall pion contamination in the electron sample was controlled to approxi-
 522 mately 2×10^{-4} or lower, with an electron efficiency above 91% during most of the
 523 data production period of the experiment. The DAQ deadtime was evaluated from a
 524 full-scale timing simulation and contributed an uncertainty of no more than 0.5% to
 525 the final asymmetry results. Systematic uncertainties from the pion contamination
 526 and the counting deadtime therefore were both negligible compared to the (3–4)%
 527 statistical uncertainty and other leading systematic uncertainties. Results presented

528 here demonstrate that accurate asymmetry measurements can be performed with
529 even higher event rates or backgrounds with this type of scaler-based DAQ.

530 **Acknowledgments**

531 This work was supported in part by the Jeffress Memorial Trust under Award
532 No. J-836, the U.S. National Science Foundation under Award No. 0653347, and
533 the U.S. Department of Energy under Award No. DE-SC0003885 and DE-AC02-
534 06CH11357. **Notice:** Authored by Jefferson Science Associates, LLC under U.S.
535 DOE Contract No. DE-AC05-06OR23177. The U.S. Government retains a non-
536 exclusive, paid-up, irrevocable, world-wide license to publish or reproduce this
537 manuscript for U.S. Government purposes.

538 **References**

- 539 [1] JLab experiment E08-011 (previously E05-007), R. Michaels, P.E. Reimer and X.-C.
540 Zheng, spokespersons.
- 541 [2] R. Subedi *et al.*, AIP proceedings of the 18th International Spin Physics Symposium
542 (2009) 245.
- 543 [3] Publications on the E08-011 physics asymmetries are in preparation.
- 544 [4] R. N. Cahn and F. J. Gilman, Phys. Rev. D **17**, 1313 (1978).
- 545 [5] K. Nakamura *et al.* [Particle Data Group], J. Phys. **G37**, 075021 (2010).
- 546 [6] J. Alcorn *et al.*, Nucl. Instrum. Meth. **A522** (2004) 294.
- 547 [7] R. Hasty *et al.* [SAMPLE Collaboration], Science **290**, 2117 (2000).
- 548 [8] K. A. Aniol *et al.* [HAPPEX Collaboration], Phys. Rev. C **69**, 065501 (2004).
- 549 [9] A. Acha *et al.* [HAPPEX Collaboration], Phys. Rev. Lett. **98**, 032301 (2007).
- 550 [10] K. A. Aniol *et al.* [HAPPEX Collaboration], Phys. Rev. Lett. **96**, 022003 (2006).
- 551 [11] K. A. Aniol *et al.* [HAPPEX Collaboration], Phys. Lett. B **635**, 275 (2006).
- 552 [12] Z. Ahmed *et al.* [HAPPEX Collaboration], Phys. Rev. Lett. **108**, 102001 (2012).
- 553 [13] S. Abrahamyan, Z. Ahmed, H. Albatineh, K. Aniol, D. S. Armstrong, W. Armstrong,
554 T. Averett and B. Babineau *et al.*, Phys. Rev. Lett. **108**, 112502 (2012).
- 555 [14] C.Y. Prescott *et al.*, Phys. Lett. **B77** (1978) 347.
- 556 [15] C.Y. Prescott *et al.*, Phys. Lett. **B84** (1979) 524.

- 557 [16] F. E. Maas *et al.* [A4 Collaboration], $Q^2 = 0.230-(\text{GeV}/c)^2$,” Phys. Rev. Lett. **93**,
558 022002 (2004).
- 559 [17] F. E. Maas, K. Aulenbacher, S. Baunack, L. Capozza, J. Diefenbach, B. Glaser,
560 T. Hammel and D. von Harrach *et al.*, $Q^2 = 0.108 (\text{GeV}/c)^2$,” Phys. Rev. Lett.
561 **94**, 152001 (2005).
- 562 [18] S. Baunack, K. Aulenbacher, D. Balaguer Rios, L. Capozza, J. Diefenbach, B. Glaser,
563 D. von Harrach and Y. Imai *et al.*, Phys. Rev. Lett. **102**, 151803 (2009).
- 564 [19] D. H. Beck, Phys. Rev. D **39**, 3248 (1989).
- 565 [20] D. S. Armstrong *et al.* [G0 Collaboration], Phys. Rev. Lett. **95**, 092001 (2005).
- 566 [21] D. Androic *et al.* [G0 Collaboration], Phys. Rev. Lett. **104**, 012001 (2010).
- 567 [22] D. Marchand, J. Arvieux, G. Batigne, L. Bimbot, A. S. Biselli, J. Bouvier, H. Breuer
568 and R. Clark *et al.* Nucl. Instrum. Meth. A **586**, 251 (2008).
- 569 [23] D. Androic *et al.* [G0 Collaboration], Nucl. Instrum. Meth. A **646**, 59 (2011).